

# Ground state and finite temperature signatures of quantum phase transitions in the half-filled Hubbard model on a honeycomb lattice

Thereza Paiva,<sup>1</sup> R.T. Scalettar,<sup>2</sup> W. Zheng,<sup>3</sup> R.R.P. Singh,<sup>2</sup> and J. Oitmaa<sup>3</sup>

<sup>1</sup> *Instituto de Física, Universidade Federal do Rio de Janeiro, Cx.P. 68.528, 21945-970 Rio de Janeiro RJ, Brazil*

<sup>2</sup> *Physics Department, University of California, Davis, CA 95616 and*

<sup>3</sup> *School of Physics, Univ. of New South Wales, Sydney NSW 2052, Australia*

(Dated: October 22, 2018)

We investigate ground state and finite temperature properties of the half-filled Hubbard model on a honeycomb lattice using quantum monte carlo and series expansion techniques. Unlike the square lattice, for which magnetic order exists at  $T = 0$  for any non-zero  $U$ , the honeycomb lattice is known to have a semi-metal phase at small  $U$  and an antiferromagnetic one at large  $U$ . We investigate the phase transition at  $T = 0$  by studying the magnetic structure factor and compressibility using quantum monte carlo simulations and by calculating the sublattice magnetization, uniform susceptibility, spin-wave and single hole dispersion using series expansions around the ordered phase. Our results are consistent with a single continuous transition at  $U_c/t$  in the range 4 – 5. Finite temperature signatures of this phase transition are seen in the behavior of the specific heat,  $C(T)$ , which changes from a two-peaked structure for  $U > U_c$  to a one-peaked structure for  $U < U_c$ . Furthermore, the  $U$  dependence of the low temperature coefficient of  $C(T)$  exhibits an anomaly at  $U \approx U_c$ .

PACS numbers: 71.10.Fd, 75.10.Lp, 75.40.Mg

## I. INTRODUCTION

The two-dimensional Hubbard Hamiltonian has been extensively studied as a model of metal–insulator and magnetic phase transitions[1] and also within the context of systems such as the  $\text{CuO}_2$  sheets of high temperature superconductors.[2] In the square-lattice case, at half-filling, nesting of the Fermi surface leads to a divergent antiferromagnetic susceptibility as the temperature is lowered, even for  $U = 0$ , and thus the ground state is an antiferromagnetic insulator at any non-zero  $U$ . It is of interest to study cases where, instead, the transition to the antiferromagnetic phase occurs at finite  $U$ . In such a situation, for example, it may prove possible to see if the Mott metal-insulator and paramagnetic–antiferromagnetic phase transitions occur separately. A finite  $U_c$  also makes it more straightforward to study the thermodynamics at temperatures above the  $T = 0$  quantum phase transition, a question pertinent to experimental studies of such phase transitions.

The two-dimensional honeycomb lattice is one geometry in which we can explore these issues. In this paper, we investigate the properties of the half-filled honeycomb lattice Hubbard model using determinant quantum monte carlo and series expansions methods. After a brief review of previous work, we describe the model and calculational approaches, and show data for a number of different ground state properties that carry signatures of the phase transition. Our overall results are consistent with a single continuous transition as a function of  $U/t$ . We then turn to the finite temperature behavior of the specific heat to see how such a critical point may be reflected in this key experimental property.

While the honeycomb lattice has  $U_c$  non-zero, it is im-

its non-interacting density of states has a special feature. As shown in Fig. 1,  $N(\omega)$  vanishes linearly as  $\omega \rightarrow 0$ , so the system is a semi-metal (or alternatively, a zero-gap semiconductor) at half-filling. As a consequence, at weak coupling, the low temperature behavior of the specific heat is quadratic in temperature,  $C = \delta T^2$ , instead of the usual linear Fermi liquid dependence. At strong coupling, when long range antiferromagnetic order sets in, the specific heat will also be quadratic in  $T$  owing to the spin-wave excitations. How the specific heat evolves between these two regimes is an open question.

A considerable body of work exists concerning the ground state phase diagram. Martelo *et al* found that within mean field theory the Mott transition occurs below an upper bound for the critical interaction strength  $U_c/t \approx 5.3$ . [3] Meanwhile, their variational monte carlo calculation suggested a lower bound for the antiferromagnetic transition  $U_c/t \approx 3.7$ . They interpreted these results as a single transition from paramagnetic metal to antiferromagnetic insulator at  $U_c/t = 4.5 \pm 0.5$ .

Baskaran *et al* [4] and Sorella *et al* [5] studied the model using the Random Phase Approximation which gives  $U_c/t = 2.23$  for the onset of antiferromagnetic order. Associated auxiliary field quantum monte carlo (QMC) simulations[5] using the ground state projection approach suggested  $U_c/t = 4.5 \pm 0.5$ . Later QMC work by Furukawa[6] on larger lattices and doing system size extrapolations resulted in a somewhat lower value,  $U_c/t = 3.6 \pm 0.1$ . Peres *et al* have recently studied the phase diagram and mean field magnetization of coupled honeycomb layers as a function of filling,  $U/t$ , and inter-layer hopping  $t'/t$  using the random phase approximation and spin wave analysis.[7]

As with the square lattice Hubbard model, Nagaoka

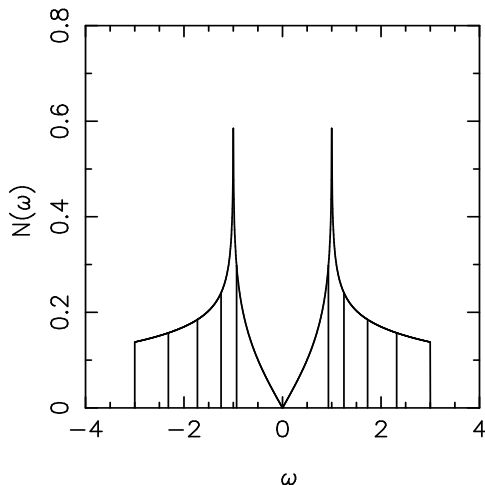


FIG. 1: The noninteracting density of states of the Hubbard model on a honeycomb lattice. This geometry is bipartite, so  $N(\omega)$  is symmetric about  $\omega = 0$ . The vertical lines correspond to fillings of 0.1, 0.2, 0.3, ... The density of states vanishes linearly at  $\omega = 0$  and has logarithmic Van Hove singularities at fillings  $\rho = 3/8$  and  $5/8$ . The bandwidth  $W = 6t$ .

lattice at strong couplings ( $U/t > 12$ ), as has been investigated by Hirsch using exact diagonalization on small clusters[8] and by Hanisch *et al* using Gutzwiller wave functions.[9]

We conclude this introduction by noting that the Hubbard model on a honeycomb lattice has also been suggested to be of interest for a variety of systems including graphite sheets,[4] and carbon nanotubes[10], as well as  $\text{MgB}_2$ [6] and Pb and Sn on Ge(111) surfaces.[11] The honeycomb lattice is also a  $2/3$  subset of the triangular lattice, and so the nature of spin correlations on the honeycomb lattice has been considered as possibly relevant to the properties of triangular lattice systems like  $\text{Na}_x\text{CoO}_2$  at appropriate dopings [12].

## II. THE HUBBARD HAMILTONIAN, DETERMINANT QUANTUM MONTE CARLO, AND SERIES EXPANSION METHODS

We study the Hubbard Hamiltonian,

$$H = -t \sum_{\langle \mathbf{i}, \mathbf{j} \rangle \sigma} (c_{\mathbf{i}\sigma}^\dagger c_{\mathbf{j}\sigma} + c_{\mathbf{j}\sigma}^\dagger c_{\mathbf{i}\sigma}) + U \sum_{\mathbf{i}} (n_{\mathbf{i}\uparrow} - \frac{1}{2})(n_{\mathbf{i}\downarrow} - \frac{1}{2}) - \mu \sum_{\mathbf{i}} (n_{\mathbf{i}\uparrow} + n_{\mathbf{i}\downarrow}).$$

Here  $c_{\mathbf{i}\sigma}^\dagger$  ( $c_{\mathbf{j}\sigma}$ ) are creation(destruction) operators for a fermion of spin  $\sigma$  on lattice site  $\mathbf{i}$ . The kinetic energy term includes a sum over near neighbors  $\langle \mathbf{i}, \mathbf{j} \rangle$  on a two-dimensional honeycomb lattice. We denote by  $N$  the number of lattice sites, and  $L$  the linear dimension with  $N = \frac{2}{3}L^2$ . The interaction term is written in particle-hole symmetric form with  $U$  the energy cost of a half-

filling: the density  $\rho = \langle n_{\mathbf{i}\uparrow} + n_{\mathbf{i}\downarrow} \rangle = 1$  for all  $t, U$  and temperatures  $T$ . We choose the hopping parameter  $t = 1$  to set the energy scale. Note that the noninteracting model has two ‘Dirac’ points  $\vec{K}_\pm$  on the Fermi surface where the dispersion relation is relativistic,[4] i.e. the energy grows linearly with  $|\vec{k} - \vec{K}_\pm|$ .

We use the determinant quantum monte carlo method to measure the properties of the Hamiltonian.[13] In this approach the partition function is written as a path integral, the interaction term is decoupled through the introduction of a discrete auxiliary ‘Hubbard-Stratonovich’ field,[14] and the fermion degrees of freedom are traced out analytically. The remaining summation over the Hubbard-Stratonovich field is done stochastically. Since the lattice is bipartite, no sign problem occurs at half-filling. Data were typically generated by doing several tens of thousands of measurements at each data point (temperature, coupling constant, lattice size). ‘Global moves’ which flip the Hubbard-Stratonovich variables for all imaginary times at a given spatial site were included so that at stronger couplings, transitions between different densities are facilitated.[15]

We have also carried out an Ising type expansion for this system at  $T = 0$  using a linked-cluster method.[16] Similar expansions were previously done for the Hubbard model on the square lattice.[17] To perform the series expansion, one needs to introduce an Ising interaction into the Hubbard Hamiltonian, and divide the Hamiltonian into an unperturbed Hamiltonian ( $H_0$ ) and a perturbation ( $H_1$ ) as follows,

$$H = H_0 + \lambda H_1$$

$$H_0 = J \sum_{\langle \mathbf{i}, \mathbf{j} \rangle} (\sigma_{\mathbf{i}}^z \sigma_{\mathbf{j}}^z + 1) + U \sum_{\mathbf{i}} (n_{\mathbf{i}\uparrow} - \frac{1}{2})(n_{\mathbf{i}\downarrow} - \frac{1}{2})$$

$$H_1 = \sum_{\langle \mathbf{i}, \mathbf{j} \rangle} [-J(\sigma_{\mathbf{i}}^z \sigma_{\mathbf{j}}^z + 1) - t(c_{\mathbf{i}\sigma}^\dagger c_{\mathbf{j}\sigma} + \text{h.c.})]$$

where  $\sigma_{\mathbf{i}}^z = n_{\mathbf{i}\uparrow} - n_{\mathbf{i}\downarrow}$ , and  $\lambda$  is the expansion parameter. Note that we are primarily interested in the behavior of the system at  $\lambda = 1$ , at which point the Ising term cancels between  $H_0$  and  $H_1$ . The strength of the Ising interaction can be varied to improve convergence, and it proves useful to keep it of order  $t^2/U$ . [17] The limits  $\lambda = 0$  and  $\lambda = 1$  correspond to the Ising model and the original model, respectively. The unperturbed ground state is the usual Neél state. The Ising series have been calculated to order  $\lambda^{15}$  for the ground state energy, the staggered magnetization  $M$ , and the square of the local moment  $L_m$ [17], and to order  $\lambda^{13}$  for the uniform magnetic susceptibility  $\chi_\perp$ . The resulting power series in  $\lambda$  for  $t/U = 0.15$  and  $J/U = 0.0225$  are presented in Table I.

In addition to the ground state properties, we also compute the spin-wave dispersion  $\Delta$  (to order  $\lambda^{13}$ ) and the dispersion  $\Delta_{1h}$  of 1-hole doped to half-filled system (to order  $\lambda^{11}$ ). The calculation of the dispersion involves a list of 28811 determinants of  $12 \times 12$  matrices. The

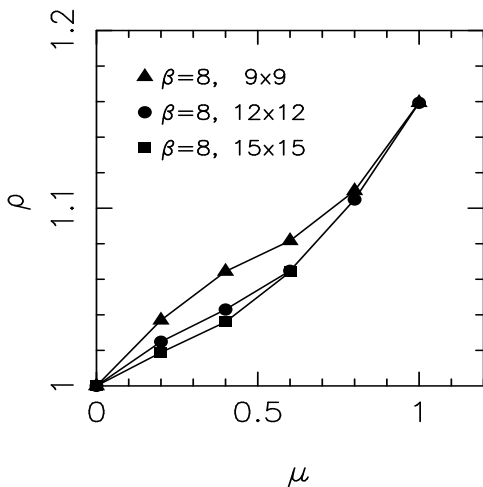


FIG. 2: Density  $\rho$  as a function of chemical potential  $\mu$  at weak coupling ( $U = 2t$ ).  $\rho$  is not pinned at one, but immediately begins to shift when  $\mu \neq 0$ : there is no Mott gap.

dispersions can be written in the following form

$$\begin{aligned} \Delta(k_x, k_y) = & \sum_p \sum_{i,j} \frac{1}{3} a_{i,j,p} \lambda^p \{ \cos(ik_x/2) \cos(\sqrt{3}jk_y/2) \\ & + \cos[(i+3j)k_x/4] \cos[\sqrt{3}(i-j)k_y/4] \\ & + \cos[(i-3j)k_x/4] \cos[\sqrt{3}(i+j)k_y/4] \} \end{aligned}$$

In Table II, we list the series coefficients  $a_{i,j,p}$  for  $t/U = 0.15$  and  $J/U = 0.0225$ . The series for other couplings are available from the authors upon request.

### III. QUANTUM PHASE TRANSITION

We begin by examining the evidence for a phase transition in the model. First, we present results from the quantum monte carlo simulations, which can, in principle, address arbitrary  $t/U$  ratios.

#### A. Compressibility

The Mott metal-insulator transition is signalled by a vanishing compressibility  $\kappa = \partial\rho/\partial\mu$ . We show  $\rho$  as a function of  $\mu$  for  $\beta = 8$  and  $U = 2t$  (Fig. 2) and  $U = 7t$  (Fig. 3). There is a clear qualitative difference in behavior. For weak coupling,  $\rho$  immediately shifts from half-filling as  $\mu$  increases from zero, while at strong coupling,  $\rho$  remains pinned at  $\rho = 1$  out to finite  $\mu$ .

In Fig. 4 we show the filling as a function of  $U$  at a small non-zero value of the chemical potential  $\mu_0 = 0.20$ . We see that  $\rho_0 \rightarrow 1$  at  $U \approx 5t$ , signalling the onset of the Mott insulating phase.

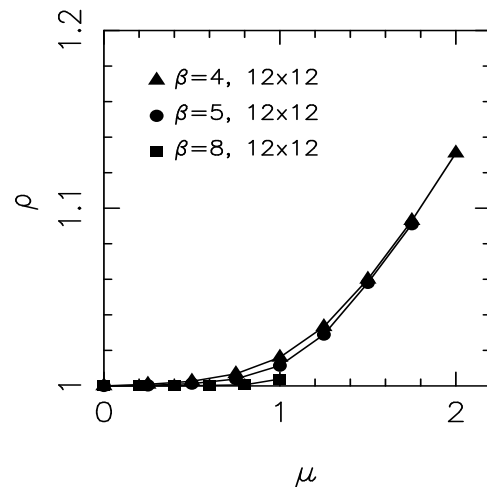


FIG. 3: Density  $\rho$  as a function of chemical potential  $\mu$  at strong coupling ( $U = 7t$ ). There is clear evidence for a Mott gap.

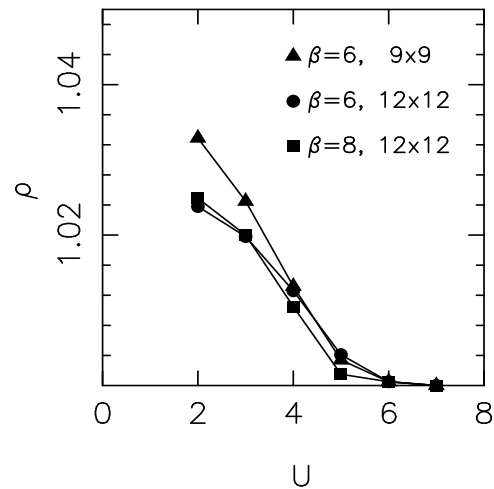


FIG. 4: The difference in the value of the density  $\rho$  from half-filling at small nonzero  $\mu_0 = 0.2t$  is a measure of the presence of the Mott gap. Here we see  $\rho(\mu_0) \rightarrow 1$  and hence a gap opens at  $U/t \approx 5$ .

#### B. Spin Correlations and Antiferromagnetic Susceptibility

To study the magnetic behavior, we measure the real space spin correlations,

$$\begin{aligned} c_{zz}(\mathbf{r}) &= \langle S_z(\mathbf{r})S_z(\mathbf{0}) \rangle & S_z(\mathbf{r}) &= n_{\mathbf{r}\uparrow} - n_{\mathbf{r}\downarrow} \\ c_{+-}(\mathbf{r}) &= \langle S_-(\mathbf{r})S_+(\mathbf{0}) \rangle & S_+(\mathbf{r}) &= c_{\mathbf{r}\uparrow}^\dagger c_{\mathbf{r}\downarrow}, \end{aligned}$$

and their Fourier transforms,

$$\begin{aligned} S_{zz}(\mathbf{q}) &= \sum_{\mathbf{r}} e^{i\mathbf{q}\cdot\mathbf{r}} c_{zz}(\mathbf{r}) \\ S_{+-}(\mathbf{q}) &= \sum_{\mathbf{r}} e^{i\mathbf{q}\cdot\mathbf{r}} c_{+-}(\mathbf{r}). \end{aligned}$$

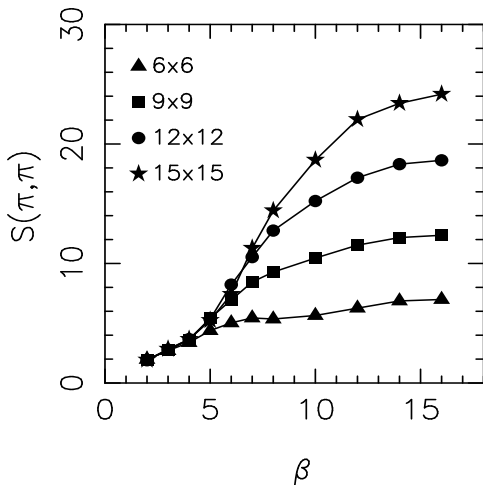


FIG. 5: The antiferromagnetic structure factor is shown as a function of inverse temperature  $\beta$  and different lattices sizes  $L$  at  $U/t = 7$ . At low  $\beta$  (high  $T$ ) the correlation length is short, and  $S(\pi, \pi)$  is independent of  $L$ . At large  $\beta$ ,  $S(\pi, \pi)$  grows with  $L$ .

At  $T = 0$  and in the antiferromagnetically ordered phase at large  $U/t$ , the real space correlation will go asymptotically to a non-zero value  $m^2/3$  at large separations  $\mathbf{r}$ . In our finite temperature simulations, we access the  $T = 0$  limit by cooling the system to the point where the correlation length exceeds the lattice size. In this case, the structure factor will grow linearly with lattice size  $N$ . More precisely, the structure factor will obey,

$$\frac{1}{N}S(\mathbf{q}) = m^2/3 + a/L,$$

where  $L$  is the linear lattice size.[18] In the paramagnetic phase at small  $U/t$ , the structure factor will be independent of  $N$ , and hence  $S(\mathbf{q})/N$  will vanish as  $N \rightarrow \infty$ .

In Fig. 5 we show  $S(\pi, \pi)$  as a function of inverse temperature  $\beta$  for different lattice sizes at  $U/t = 7$ . Fig. 6 shows the associated scaling plot. Also shown in Fig. 6 is the value of  $c(\mathbf{r})$  for the largest separations on our finite lattices. This quantity should scale with the same intercept  $m^2/3$  but a different finite size correction. We see that the system is in an antiferromagnetically ordered phase for this coupling.

Figs. 7-8 show analogous plots at  $U/t = 6$ . The order parameter is still non-zero, but is quite small. Similar plots for  $U/t = 5$  are consistent with the vanishing of long range order. While we cannot pin down the location of the quantum phase transition exactly, a comparison of this analysis with the compressibility of Fig. 3 suggests that the vanishing of the compressibility gap and the antiferromagnetic order occur very close to each other and

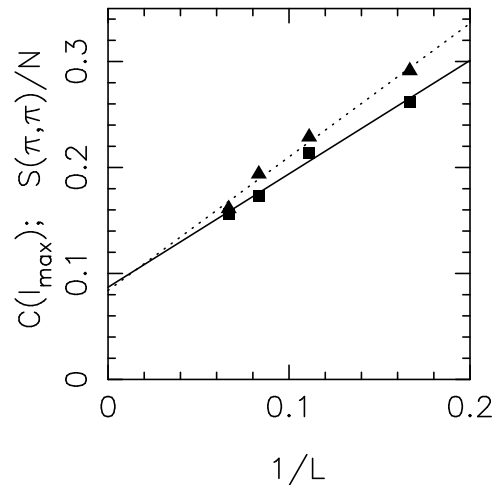


FIG. 6: The scaled structure factor (filled triangles) and spin correlation function (filled squares) at large distance are shown for large  $\beta$  as a function of the inverse linear dimension for  $U/t = 7$ . The lines are least squares fits to the data. These quantities scale to a nonzero value of the order parameter (square of the staggered magnetization) in the thermodynamic limit  $1/L \rightarrow 0$ .

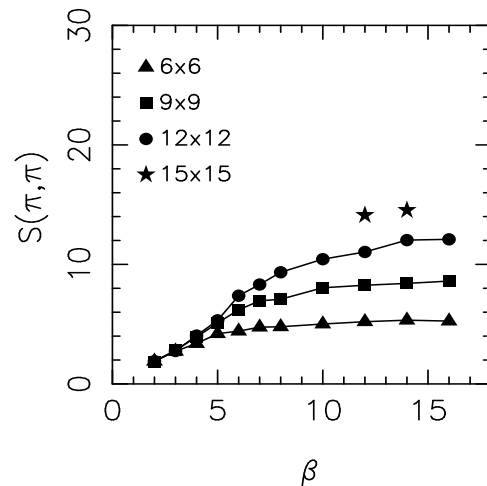


FIG. 7: Same as Fig. 5 except  $U/t = 6$ .

### C. Results from Series Expansions

We now present results from the Ising type series expansions. These expansions are only valid in the magnetically ordered phase, and thus can only access the properties of the system for  $U > U_c$ .

In Fig. 9 and Fig. 10, we show the sublattice magnetization and uniform susceptibility. The QMC results for the sublattice magnetization are also shown. The two agree with each other for small  $t/U$ . The uncertainties increase as the transition is approached. QMC results suggest a more abrupt drop to zero around  $U/t \approx 5$ , whereas the series results suggest a gradual decrease with increasing  $t/U$ . Since the series expansion is only valid in the

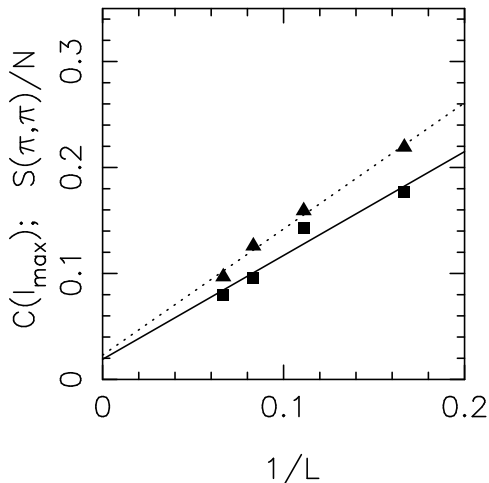


FIG. 8: Same as Fig. 6 except  $U/t = 6$ .

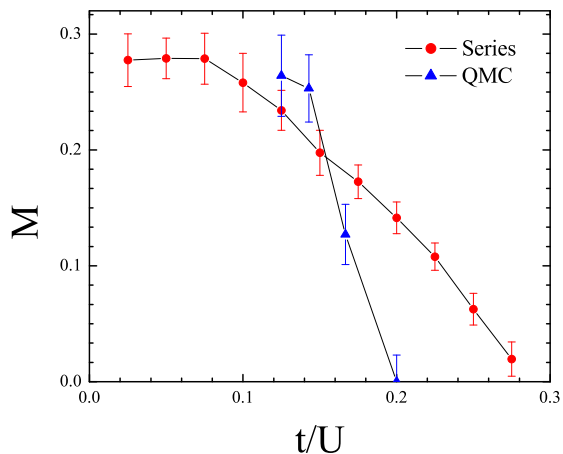


FIG. 9: The staggered magnetization versus  $t/U$  obtained from series expansions and quantum monte carlo simulations. The lines joining the points are a guide to the eye. See text for more discussion.

variable  $t/U$  but rather in an auxiliary variable  $\lambda$ , it is difficult to locate the true critical point  $U_c/t$  and obtain the critical properties. However, since we expect the critical exponent  $\beta$  to be less than one, the true curve should come to zero with an infinite slope. Thus, from the series results alone, one would estimate  $U_c/t \approx 4$ , and this is in agreement with the estimate from the susceptibility  $\chi_{\perp}$  shown in Fig. 10.

Next, in Fig. 11, we show the spin-wave dispersion along high-symmetry cuts through the Brillouin zone for  $t/U = 0.1$ , together with the dispersion obtained from first and second order spin-wave results for the Heisenberg model on a honeycomb lattice[19], which should approach the dispersion for the Hubbard model in the large  $U$  limit. We can see that the dispersion has its minimum at the  $F$  point. The dispersion relation for the Heisenberg

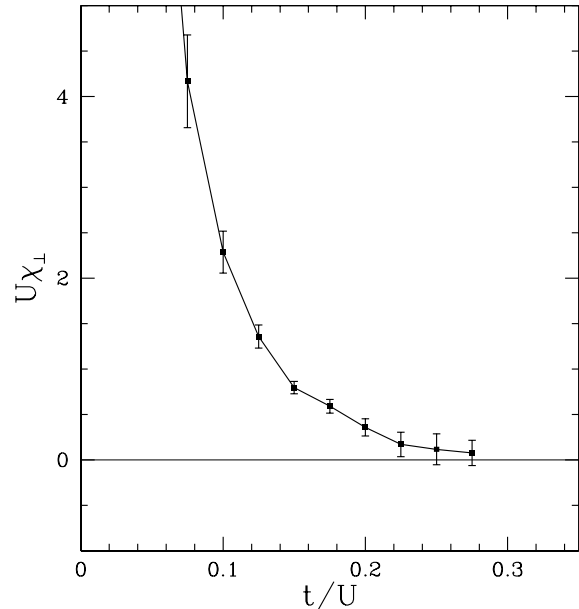


FIG. 10: The uniform susceptibility  $U\chi_{\perp}$  versus  $t/U$  obtained from series expansion.

berg model on a honeycomb lattice has a maximum at  $W$  point, while for the Hubbard model, this is only true for very small  $t/U$ . Already for  $t/U = 0.1$ , the energy at  $W$  points is reduced, and the maximum moves to the  $K$  point.

Also, in figure 12 we show the 1-hole dispersion for selected values of  $t/U$ , where we can see that the minimum and maximum gaps are at the  $W$  and  $\Gamma$  points, respectively. This dispersion is quite different from the case of the square lattice, since there is no nesting of the Fermi surface here. For the square lattice, the single hole dispersion relation is anomalously flat near the degenerate points  $(0, \pm\pi)$ ,  $(\pm\pi, 0)$  of the Brillouin zone, with the minimum of the dispersion at  $(\pm\pi/2, \pm\pi/2)$ . [20] Fig. 13 shows the minimum gap, i.e. the gap at the  $W$  point, and the bandwidth,  $\Delta_{\Gamma} - \Delta_W$ , vs  $t/U$ . The gap closes at  $t/U \approx 0.26$ , indicating a transition to the semi-metal phase.

To summarize, study of both magnetic and charge properties using series expansions show a direct transition from the antiferromagnetic to the semi-metal phase around  $U_c \approx 4t$ .

Combining the quantum monte carlo and series expansion results, we estimate the phase transition to be in the range  $U_c/t = 4 - 5$ . There is greater internal consistency in the location of the critical point if we restrict ourselves to one method. But, in fact, there are larger uncertainties in both methods especially as the quantum phase transition is reached. However, both methods strongly indicate that the Mott transition and the antiferromagnetic order

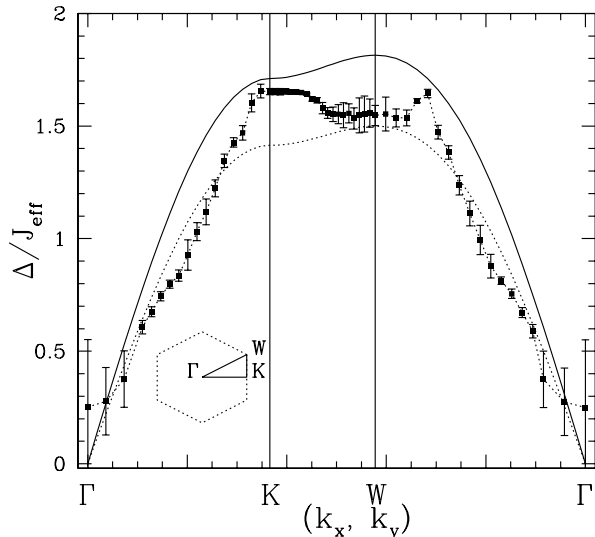


FIG. 11: Plot of the spin-wave excitation spectrum  $\Delta(k_x, k_y)$  (in units of effective  $J_{\text{eff}} = 4t^2/U$ ) along the path  $\Gamma KW\Gamma$  in the Brillouin zone (see the inset, where the momentum  $\mathbf{k}$  for  $\Gamma$ ,  $K$ ,  $W$  points are  $(0, 0)$ ,  $(2\pi/3, 0)$ , and  $(2\pi/3, 2\pi/3\sqrt{3})$ , respectively) for the system with coupling ratios  $t/U = 0.1$  in the Néel ordered phase. Also shown are the first (dashed line) and second (solid line) order spin-wave results[19] for Heisenberg model on honeycomb lattice.

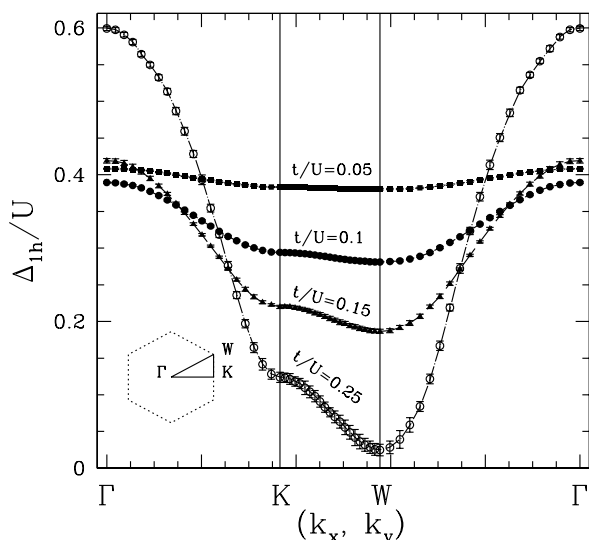


FIG. 12: Plot of the 1-hole excitation spectrum  $\Delta_{1h}(k_x, k_y)/U$  in the Néel ordered phase along the path  $\Gamma KW\Gamma$  in the Brillouin zone (see the inset) for the system with coupling ratios  $t/U = 0.05, 0.1, 0.15, 0.25$ .

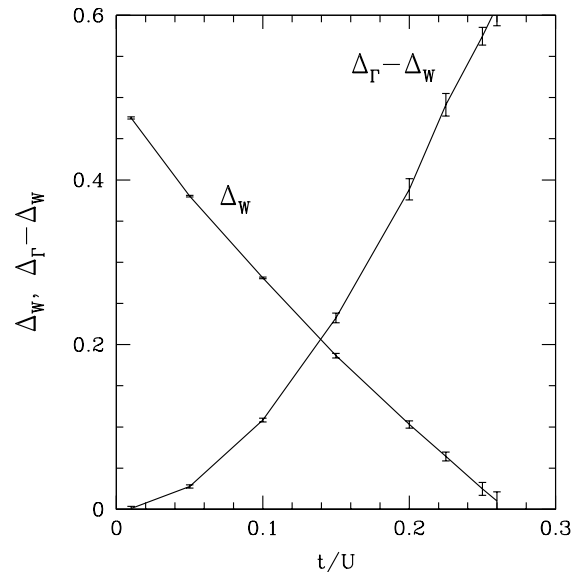


FIG. 13: The minimum single-hole gap  $\Delta_W$  at  $W$  point and its bandwidth  $\Delta_\Gamma - \Delta_W$  vs  $t/U$ .

#### IV. SIGNATURES OF THE QUANTUM PHASE TRANSITION IN THE SPECIFIC HEAT

An important objective of our study was to examine the signature of the quantum phase transition in the finite temperature behavior of the specific heat. We now turn to those studies, which are based on the quantum monte carlo method.

At strong couplings, one expects two features in the specific heat of the Hubbard Hamiltonian. The first, at a temperature  $T \approx U/5$ , signals the formation of magnetic moments,[21, 22] while the second, at a lower temperature  $T \approx J = 4t^2/U$ , is associated with the entropy of moment ordering. This picture has been verified in the one-dimensional case using Bethe Ansatz techniques[23] and (using quantum monte carlo) in the two dimensional square[24, 25] and three dimensional cubic lattices.[26] Interestingly, in the square lattice, the two peak structure persists to weak coupling where the energy scales  $U$  and  $J$  have merged.[21] In one dimension, there is a single peak at weak coupling.[27, 28]

The specific heat  $C(T)$  for the two-dimensional honeycomb lattice is shown in Fig. 16 for different couplings  $U$  and lattice size  $L = 12$ . For strong coupling,  $U/t = 6, 7, 8$  there is a clear two peak structure. This is replaced by a single peak for weaker couplings,  $U/t = 2, 4, 5$ . Again, this result is in contrast with the behavior of  $C(T)$  on the square lattice, where a two-peak structure is evident for all  $U/T$ . [21] It is plausible to conjecture that the difference is the absence of long range antiferromagnetic order. This suggestion is supported by the fact that coalescence of the specific heat peaks is seen in “Dynamical Mean Field Theory” (DMFT) [29, 30, 31] studies on the

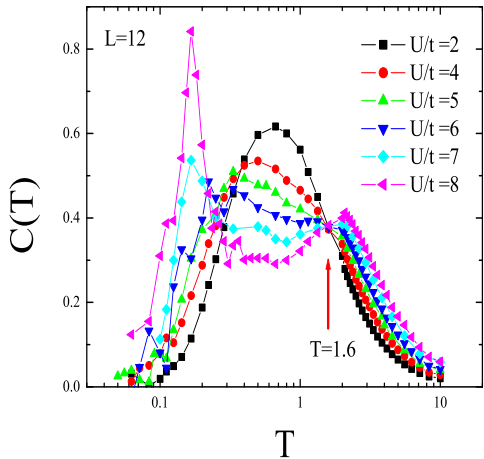


FIG. 14: The specific heat  $C(T)$  is shown as a function of temperature for different coupling strengths. In the antiferromagnetic phase for  $U > U_c$ , the specific heat has a two peak structure. In the metallic phase for  $U < U_c$  there is a single peak. The ‘universal crossing’ at  $T = 1.6t$  is discussed in the text.

are restricted to the paramagnetic phase and antiferromagnetic fluctuations are neglected.

This is, however, a rather subtle question, since the Mermin–Wagner theorem precludes long range order at finite temperature. What is meant, more precisely, is that on a two-dimensional square lattice, the low  $T$  structure in  $C(T)$  appears when the antiferromagnetic correlation length  $\xi(T)$ , begins to grow exponentially as  $T \rightarrow 0$ .

The evolution from a two to a one peak structure in  $C(T)$  is one interesting reflection of the underlying quantum phase transition on the finite temperature thermodynamics. Another way of examining this question concerns the low temperature behavior of  $C(T)$ . As pointed out in the introduction, we expect a quadratic temperature dependence at both strong coupling (spin-waves) and weak coupling (linearly vanishing density of states at the Fermi level). How does the coefficient  $\delta$  in  $C(T) = \delta T^2$  evolve as one crosses between the two phases?

Before we present the results for  $\delta$ , we note that extracting  $\delta$  is clearly a subtle numerical issue. On the one hand,  $\delta$  characterizes the low  $T$  behavior, but on the other hand, because of finite size effects, which become larger as the temperature is lowered, one cannot use data at too low values of  $T$ . Thus, our calculation of  $\delta$  should be viewed with some caution. What we have done in generating Figs. 15-16 is to fit the data for  $C(T)$  to the  $T^2$  form over only a finite temperature window: below the peak in  $C(T)$  but also above the temperatures at which finite size effects begin introducing a noticeable gap in the spectrum. In Fig. 15 we show  $\delta$  as a function of  $U$ . The important point in this plot is the vicinity of the

value  $U_c/t \approx 5$  previously inferred from the compressibility and spin correlation data. Fig. 16 emphasizes this feature by plotting the derivative of  $\delta$  with respect to  $t/U$  as a function of  $t/U$ . As we have noted, the specific heat of the noninteracting system obeys  $C = \delta(U = 0)T^2$  with  $\delta(U = 0) = 4.1$ , because of the linearly vanishing density of states. Perturbation theory suggests that for small finite  $U$ ,  $\delta$  should increase quadratically from this value. Nevertheless, in the vicinity below the quantum phase transition, the value for  $\delta$  extracted from the quantum monte carlo data looks rather linear in  $U$ , as seen in Fig. 15. If  $\delta = mU/t$  then  $d(\delta)/d(t/U) = -m/(t/U)^2$ . With this in mind, a line showing the functional form  $-m/(t/U)^2$  with  $m = 2$  is given and fits the weak coupling data very well. The breakaway from this form at strong coupling further emphasizes the change in behavior in the vicinity of the quantum phase transition.

In studies of the two peak structure of the specific heat on the square lattice, an interesting interchange of the role of kinetic and potential energies was noted.[21] At large  $U$ , the temperature derivative of the potential energy was the primary contribution to the high  $T$ , ‘moment formation’, peak, while the temperature derivative of the kinetic energy drove the low  $T$ , ‘moment ordering’, peak. However, at weak  $U$  the situation was reversed, with the high  $T$  peak originating in the kinetic energy. With that separation in mind, we plot in Fig. 17, for the honeycomb lattice, the contributions of the potential and kinetic energies to  $\delta$ . It is the contribution of the potential energy to  $\delta$  which appears to have the sharper evolution in the vicinity of the quantum phase transition.

Returning to the specific heat versus temperature, shown in Fig. 14, we note the existence of a very well defined crossing point at  $T \approx 1.6t$ . This crossing has been observed previously in DMFT,[29, 30, 31] and in the two dimensional square lattice.[21, 24] Indeed, in the former case, two crossings were observed, with the high temperature one being nearly universal, while the low temperature intersections were considerably more spread out, much as we observe in Fig. 14. It is also interesting that the numerical value of the crossing is almost identical for the honeycomb and square lattices, despite their different bandwidths.

Finally, we turn to the behavior of the entropy  $S$ . In Fig. 18 we show  $S$  as a function of  $U$  for different temperatures  $T$ . At large  $U$ , the clustering of the curves for different temperatures near  $\ln(2)$  is indicative of the existence of disordered magnetic moments in a range of intermediate  $T$ . The low temperature magnetic ordering tendency is evident in the gap between the  $T = 0.2$  and  $T = 0.3$  curves. As  $U$  is decreased, the screening away of the moments is indicated by the  $T = 0.3$  isotherm dropping from  $\ln(2)$  to 0. It is interesting that this behavior is so gradual. Finally at small  $U$  one observes the more or less equally spaced isotherms of free electron gas. This figure complements the data of  $C(T)$  shown in Fig. 14, since the entropy hang up at large  $U$  near  $\ln(2)$  is just the  $C(T)$  for the disordered magnetic moments.

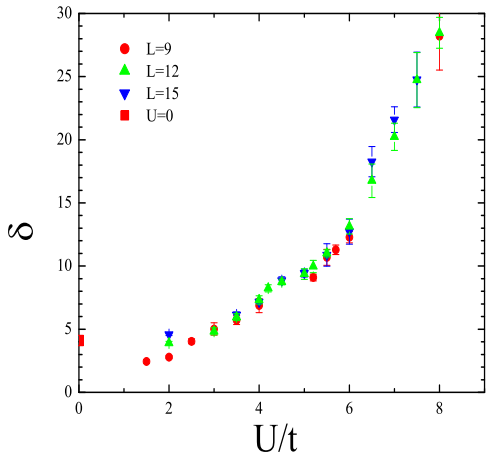


FIG. 15:  $\delta$ , the coefficient of the  $T^2$  term in the specific heat is shown as a function of  $U/t$ . The solid square is the  $U = 0$  value. There appears to be a change in slope as  $U$  crosses  $U_c$ .

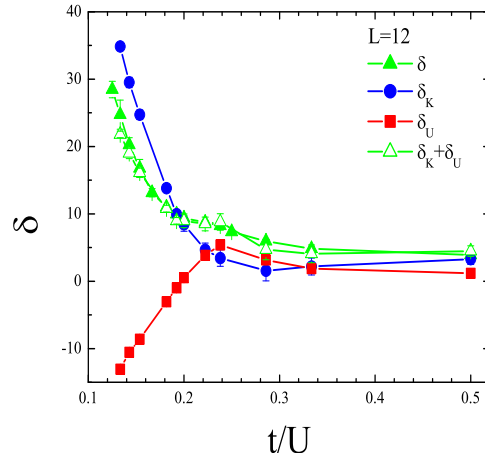


FIG. 17: The separate contributions of the potential ( $\delta_U$ ) and kinetic ( $\delta_K$ ) energies to the quadratic coefficient of the specific heat are shown.  $\delta_U$  shows the more abrupt behavior in the vicinity of  $U_c$ . The small differences between the values of  $\delta$  obtained from the total energy, and the values  $\delta_K + \delta_U$  from the kinetic and potential energies separately provide a measure of the uncertainties in our fitting procedure.

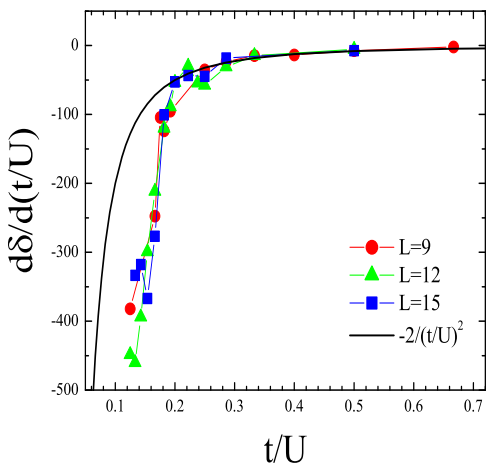


FIG. 16: The derivative of  $\delta$ , the coefficient of the  $T^2$  term in the specific heat, with respect to  $t/U$  is shown. This derivative has a sharp change near the critical coupling  $U_c$ . The solid line is  $-2/(t/U)^2$  (see text).

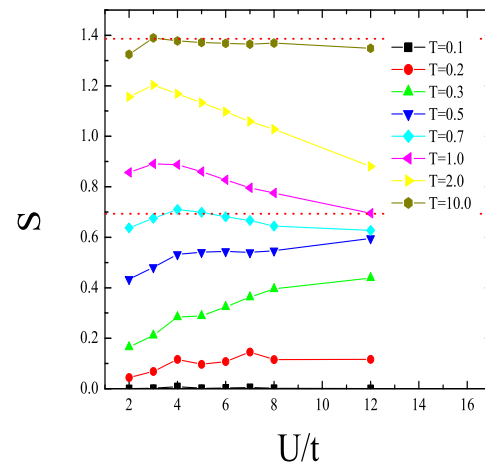


FIG. 18: The entropy is shown as a function of  $U$  for different temperatures. At large  $U$  the gaps between the  $T = 10$  and  $T = 2$  curves and between the  $T = 0.3$  and  $T = 0.2$  curves reflect the entropy loss associated with magnetic moment formation and ordering respectively.

## V. CONCLUSIONS

Figure 19 exhibits the entropy as a function of temperature. At weak coupling, there is a smooth evolution from  $\ln(4)$  at high  $T$  to zero at low  $T$ . For strong coupling, a plateau near  $\ln(2)$  interrupts this evolution, again exhibiting a range of temperatures with well formed, but

In this paper we have studied the Hubbard Hamiltonian on a half-filled honeycomb lattice using quantum monte carlo and series expansion methods. Both methods strongly suggest that the model has a single con-



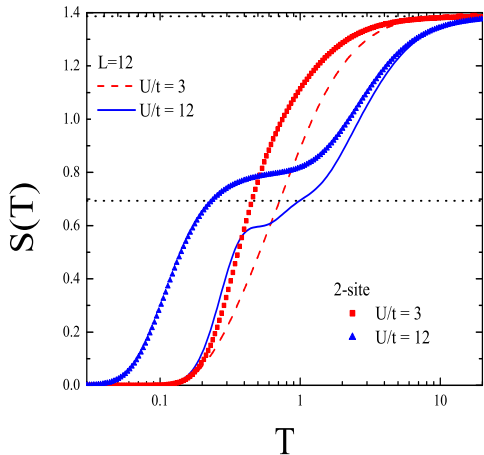


FIG. 19: The entropy is shown as a function of  $T$  for weak and strong coupling. The dashed and solid lines are the results of quantum monte carlo simulations on  $12 \times 12$  lattices. The symbols are generated by an exact calculation on a two site model for comparison.

netic phase at large  $U/t$  and a semi-metal phase at small  $U/t$ . Quantum monte carlo results for the compressibility, which looks at the charge response of the system, and the magnetic structure factor, which looks at the spin response, both suggest a transition around  $U_c/t \approx 5$ . The series expansion results for the sublattice magnetization, which is the spin order parameter and the charge excitation gap, which characterizes the Mott transition, both point to a single transition at  $U/t \approx 4$ . The discrepancy between the quantum monte carlo and series expansion results reflects the uncertainties in the calculations, especially as the critical point is approached. Thus we expect the transition to lie in the range  $4 < U/t < 5$ , a result in complete agreement with the previous work of Martelo et al. [3].

Finally, one of the goals of this work was to look for

finite temperature signatures of the phase transition in the specific heat, as a guide to experimental studies. We observe that around  $U_c$  the specific heat changes from a one peak (below  $U_c$ ) to a two peak (above  $U_c$ ) structure. We suggest that this is associated with the fact that for  $U > U_c$  the antiferromagnetic correlation length grows rapidly as the temperature is reduced. For weak coupling only very short-range antiferromagnetic correlations exist, and the specific heat has no signature of magnetic order.

We also studied the evolution with on-site interaction strength  $U$  of the coefficient  $\delta(U)$  of the quadratic temperature dependence of the specific heat at low temperatures. Since the excitations which produce the  $T^2$  term above and below the quantum phase transition are unrelated, one might have expected  $\delta(U)$  to exhibit a discontinuity at  $U_c$ . Instead, we found a sharp change in the slope,  $d\delta(U)/dU$  at  $U_c$ . Given the uncertainties in obtaining  $\delta(U)$ , from finite-size calculations, these results should be viewed with some caution. Experimental searches for such a behavior would be quite interesting.

### Acknowledgments

We acknowledge very useful conversations with W.E. Pickett and A.K. McMahan. This work was supported by the CNPq-Brazil and FUJB-Brazil (TP), US National Science Foundation grants DMR-0312261 (RTS), INT-0203837 (RTS), and DMR-0240918 (RRPS), and by a grant from the Australian Research Council (WZ and JO). W.Z. wishes to thank the University of California at Davis for hospitality while part of the work was being done. We are grateful for the computing resources provided by the Australian Centre for Advanced Computing and Communications (AC3) and by the Australian Partnership for Advanced Computing (APAC) National Facility.

- 
- [1] See *The Hubbard Model*, A. Montorsi, ed, World Scientific (1992); *The Hubbard Model—Recent Results* M. Rasetti, ed, World Scientific (1991); and references therein.
- [2] D.J. Scalapino, in Does the Hubbard model have the right stuff?, edited by R.A. Broglia and J.R. Schrieffer, Proceedings of the International School of Physics, Enrico Fermi, Course CXXI (North-Holland, Amsterdam, 1994).
- [3] L.M. Martelo, M. Dzierzawa, L. Siffert, and D. Baeriswyl, Z. Phys. B **103**, 335 (1997).
- [4] G. Baskaran and S.A. Jafari, Phys. Rev. Lett. **89**, 016402 (2002).
- [5] S. Sorella and E. Tosatti, Europhys. Lett. **19**, 699 (1992).
- [6] N. Furukawa, J. Phys. Soc. Japan **70**, 1483 (2001).
- [7] N.M.R. Peres, M.A.N. Araujo, and D. Bozi, Phys. Rev. B **60**, 080405 (1999).
- [8] R. Hirsch, Ph.D. thesis, Univ. of Cologne (1994).
- [9] T. Hanisch, B. Kleine, A. Ritzl, and E. Müller-Hartmann, Ann. Phys. (Leipzig), **4**, 303 (1995).
- [10] L. Balents and M.P.A. Fisher, Phys. Rev. B **55**, R11973 (1997).
- [11] <http://cst-www.nrl.navy.mil/hellberg/projects/csh.html>
- [12] See for example, W. Zheng, J. Oitmaa, C.J. Hamer and R.R.P. Singh, cond-mat/0403718.
- [13] R. Blankenbecler, R.L. Sugar, and D.J. Scalapino, Phys. Rev. D **24**, 2278 (1981).
- [14] J.E. Hirsch, Phys. Rev. B **31**, 4403 (1985).
- [15] R.T. Scalettar, R.M. Noack, and R.R.P. Singh, Phys. Rev. **B44**, 10502 (1991).
- [16] M.P. Gelfand and R.R.P. Singh, Adv. Phys. **49**, 93(2000).
- [17] Z.D. Si, L.D. D. Singh, Phys. Rev. B **50**, 9690 (1995).

TABLE I: Series coefficients for Ising expansions of the ground-state energy per site,  $E_0/NU$ , the staggered magnetization  $M$ , squared local moment  $L_m$ , and the uniform magnetic susceptibility  $\chi_\perp$  for  $t/U = 0.15$  and  $J/U = 0.0225$ . Coefficients of  $\lambda^n$  up to order  $\lambda^{15}$  are listed.

$n$	$E_0/NU$	$M$	$L_m$	$\chi_\perp$
0	-0.250000000	1.000000000	1.000000000	3.703703704
1	0.000000000	0.000000000	0.000000000	3.703703704
2	$-6.067415730 \times 10^{-2}$	$-1.090771367 \times 10^{-1}$	$-1.090771367 \times 10^{-1}$	-4.743810362
3	$-6.135588941 \times 10^{-3}$	$-2.206054451 \times 10^{-2}$	$-2.206054451 \times 10^{-2}$	$-1.394196294 \times 10^1$
4	$-1.172455577 \times 10^{-2}$	$-3.552865175 \times 10^{-1}$	$-3.819372077 \times 10^{-2}$	-5.304439204
5	$-1.595132209 \times 10^{-2}$	$-7.348348039 \times 10^{-1}$	$-6.041765980 \times 10^{-2}$	$2.402576623 \times 10^1$
6	$-2.167350013 \times 10^{-3}$	$-4.545288062 \times 10^{-1}$	$1.617075260 \times 10^{-2}$	$3.836014584 \times 10^1$
7	$1.484188843 \times 10^{-2}$	$5.706090877 \times 10^{-1}$	$1.182931503 \times 10^{-1}$	-6.261816470
8	$1.982803975 \times 10^{-2}$	1.508870723	$1.282196638 \times 10^{-1}$	$-8.556886959 \times 10^1$
9	$1.098873088 \times 10^{-2}$	1.362697325	$2.870390056 \times 10^{-2}$	$-8.473956953 \times 10^1$
10	$-5.309942069 \times 10^{-3}$	$-9.038107499 \times 10^{-2}$	$-1.194968503 \times 10^{-1}$	$7.394366538 \times 10^1$
11	$-2.087445585 \times 10^{-2}$	-1.988476084	$-2.381637820 \times 10^{-1}$	$2.479347440 \times 10^2$
12	$-2.733805940 \times 10^{-2}$	-2.967041815	$-2.434002720 \times 10^{-1}$	$1.283247884 \times 10^2$
13	$-1.868451700 \times 10^{-2}$	-2.220001906	$-7.558507985 \times 10^{-2}$	$-3.404916769 \times 10^2$
14	$4.985233235 \times 10^{-3}$	$-1.210494842 \times 10^{-2}$	$2.437663805 \times 10^{-1}$	
15	$3.577717123 \times 10^{-2}$	2.934366446	$5.886265926 \times 10^{-1}$	

- [18] D.A. Huse, Phys. Rev. B **37**, 2380 (1988).  
[19] W. Zheng, J. Oitmaa and C.J. Hamer, Phys. Rev. B **44**, 11869 (1991).  
[20] See for example, C. J. Hamer, Zheng Weihong, and J. Oitmaa, Phys. Rev. B **58**, 15508 (1998).  
[21] T. Paiva, C. Huscroft, A.K. McMahan, and R.T. Scalettar, Phys. Rev. B **63**, 125116 (2001).  
[22] See also Fig. 36 in A. Georges *et al* Rev. Mod. Phys. **68**, 13 (1996).  
[23] M. Takahashi, Prog. Theor. Phys. **52**, 103 (1974).  
[24] D. Duffy and A. Moreo, Phys. Rev. B **55**, 12918 (1997).  
[25] R. Staudt, M. Dzierzawa, and A. Muramatsu, Eur. Phys. J. B **17**, 411 (2000).  
[26] R. T. Scalettar, D. J. Scalapino, R. L. Sugar, and D. Toussaint, Phys. Rev. B **39**, 4711 (1989).  
[27] H. Shiba and P.A. Pincus, Phys. Rev. B **5**, 1966 (1972).  
[28] J. Schulte and M. Böhm, Phys. Rev. B **53**, 15385 (1996).  
[29] A. Georges and W. Krauth, Phys. Rev. B **48**, 7167 (1993).  
[30] D. Vollhardt, Phys. Rev. Lett. **78**, 1307 (1997).  
[31] N. Chandra, M. Kollar, and D. Vollhardt, Phys. Rev. B **59**, 10541 (1999).

TABLE II: Series coefficients for the spin-wave excitation spectrum  $\Delta(k_x, k_y)/U$  and 1-hole dispersion  $\Delta_{1h}(k_x, k_y)/U$ . Nonzero coefficients up to order  $\lambda^{13}$  for  $t/U = 0.15$  and  $J/U = 0.0225$  are listed.

$(i, j, p)$	$a_{i,j,p}$	$(i, j, p)$	$a_{i,j,p}$	$(i, j, p)$	$a_{i,j,p}$	$(i, j, p)$	$a_{i,j,p}$
spin-wave excitation spectrum $\Delta(k_x, k_y)/U$							
(0, 0, 0)	$1.350000000 \times 10^{-1}$	(10, 0, 0)	$2.216091139 \times 10^{-1}$	(10, 3, 1)	$4.746162497 \times 10^{-1}$	(8, 6, 0)	$-7.225113429 \times 10^{-3}$
(1, 0, 0)	$-1.350000000 \times 10^{-1}$	(11, 0, 0)	$-1.393969235 \times 10^{-2}$	(11, 3, 1)	$-1.099204748 \times 10^{-1}$	(9, 6, 0)	$-2.262498583 \times 10^{-2}$
(2, 0, 0)	$1.111175434 \times 10^{-1}$	(12, 0, 0)	$-5.637616584 \times 10^{-1}$	(12, 3, 1)	$-1.440323067$	(10, 6, 0)	$-2.696906952 \times 10^{-2}$
(3, 0, 0)	$2.082046617 \times 10^{-2}$	(13, 0, 0)	$-1.304334460$	(13, 3, 1)	$-3.353557841$	(11, 6, 0)	$6.591260743 \times 10^{-3}$
(4, 0, 0)	$-4.424242442 \times 10^{-2}$	(4, 3, 1)	$-1.237981890 \times 10^{-1}$	(8, 6, 2)	$-3.350958277 \times 10^{-3}$	(12, 6, 0)	$-2.916010244 \times 10^{-3}$
(5, 0, 0)	$-3.676674665 \times 10^{-2}$	(5, 3, 1)	$-1.341231436 \times 10^{-1}$	(9, 6, 2)	$-1.098231382 \times 10^{-2}$	(13, 6, 0)	$-2.568183304 \times 10^{-1}$
(6, 0, 0)	$-9.749111612 \times 10^{-3}$	(6, 3, 1)	$-2.171649093 \times 10^{-2}$	(10, 6, 2)	$-1.153863507 \times 10^{-2}$	(12, 9, 3)	$-1.609104960 \times 10^{-3}$
(7, 0, 0)	$2.153747460 \times 10^{-2}$	(7, 3, 1)	$1.086787464 \times 10^{-1}$	(11, 6, 2)	$7.460180712 \times 10^{-3}$	(13, 9, 3)	$-8.451196579 \times 10^{-3}$
(8, 0, 0)	$9.813204715 \times 10^{-2}$	(8, 3, 1)	$2.930587649 \times 10^{-1}$	(12, 6, 2)	$7.410248941 \times 10^{-3}$	(12, 9, 1)	$-9.742145152 \times 10^{-3}$
(9, 0, 0)	$2.080499557 \times 10^{-1}$	(9, 3, 1)	$5.034160236 \times 10^{-1}$	(13, 6, 2)	$-1.092694552 \times 10^{-1}$	(13, 9, 1)	$-5.101138671 \times 10^{-2}$
1-hole dispersion $\Delta_{1h}(k_x, k_y)/U$							
(0, 0, 0)	$5.675000000 \times 10^{-1}$	(7, 3, 1)	$5.141564645$	(8, 6, 0)	$-1.091561629$	(9, 12, 4)	$-2.562349516 \times 10^{-6}$
(1, 0, 0)	$-6.750000000 \times 10^{-2}$	(8, 3, 1)	$-1.258196166 \times 10^1$	(9, 6, 0)	$-5.455143302$	(10, 12, 4)	$2.676464885 \times 10^{-3}$
(2, 0, 0)	$-6.336614782 \times 10^{-1}$	(9, 3, 1)	$-1.733463014 \times 10^2$	(10, 6, 0)	$5.327561412$	(11, 12, 4)	$1.433265640 \times 10^{-2}$
(3, 0, 0)	$-7.336392902 \times 10^{-1}$	(10, 3, 1)	$-6.526403290 \times 10^1$	(11, 6, 0)	$8.443452858 \times 10^1$	(8, 12, 2)	$-2.978280918 \times 10^{-5}$
(4, 0, 0)	$2.938067768$	(11, 3, 1)	$3.901815114 \times 10^3$	(6, 9, 3)	$8.189533379 \times 10^{-5}$	(9, 12, 2)	$-2.049879613 \times 10^{-5}$
(5, 0, 0)	$1.013199055 \times 10^1$	(4, 6, 2)	$-2.251112570 \times 10^{-3}$	(7, 9, 3)	$3.983472192 \times 10^{-5}$	(10, 12, 2)	$2.139465782 \times 10^{-2}$
(6, 0, 0)	$-1.702110647 \times 10^1$	(5, 6, 2)	$-6.420330616 \times 10^{-4}$	(8, 9, 3)	$1.025604453 \times 10^{-2}$	(11, 12, 2)	$1.146460686 \times 10^{-1}$
(7, 0, 0)	$-1.514268463 \times 10^2$	(6, 6, 2)	$2.127063569 \times 10^{-2}$	(9, 9, 3)	$4.129584046 \times 10^{-2}$	(8, 12, 0)	$-2.233710688 \times 10^{-5}$
(8, 0, 0)	$-4.655833834$	(7, 6, 2)	$6.346958017 \times 10^{-2}$	(10, 9, 3)	$-2.110091800 \times 10^{-1}$	(9, 12, 0)	$-1.537409710 \times 10^{-5}$
(9, 0, 0)	$2.217144323 \times 10^3$	(8, 6, 2)	$-5.148299650 \times 10^{-1}$	(11, 9, 3)	$-1.677872051$	(10, 12, 0)	$1.604362363 \times 10^{-2}$
(10, 0, 0)	$3.740789745 \times 10^3$	(9, 6, 2)	$-2.603465931$	(6, 9, 1)	$4.913720027 \times 10^{-4}$	(11, 12, 0)	$8.598244287 \times 10^{-2}$
(11, 0, 0)	$-2.947388888 \times 10^4$	(10, 6, 2)	$2.034643910$	(7, 9, 1)	$2.390083315 \times 10^{-4}$	(10, 15, 5)	$1.895585905 \times 10^{-7}$
(2, 3, 1)	$1.238532110 \times 10^{-1}$	(11, 6, 2)	$3.720022590 \times 10^1$	(8, 9, 1)	$6.168519384 \times 10^{-2}$	(11, 15, 5)	$1.687061931 \times 10^{-7}$
(3, 3, 1)	$1.022641192 \times 10^{-2}$	(4, 6, 0)	$-4.502225139 \times 10^{-3}$	(9, 9, 1)	$2.478775229 \times 10^{-1}$	(10, 15, 3)	$1.895585905 \times 10^{-6}$
(4, 3, 1)	$7.872629131 \times 10^{-2}$	(5, 6, 0)	$-1.284066123 \times 10^{-3}$	(10, 9, 1)	$-1.373111288$	(11, 15, 3)	$1.687061931 \times 10^{-6}$
(5, 3, 1)	$8.219599490 \times 10^{-3}$	(6, 6, 0)	$4.204959522 \times 10^{-2}$	(11, 9, 1)	$-1.064077735 \times 10^1$	(10, 15, 1)	$3.791171810 \times 10^{-6}$
(6, 3, 1)	$6.643492076 \times 10^{-1}$	(7, 6, 0)	$1.267005690 \times 10^{-1}$	(8, 12, 4)	$-3.722851147 \times 10^{-6}$	(11, 15, 1)	$3.374123863 \times 10^{-6}$